

UCRL-JRNL-233964



LAWRENCE  
LIVERMORE  
NATIONAL  
LABORATORY

# Quantifying the effects of three-dimensional subsurface heterogeneity on Hortonian runoff processes using a fully-coupled numerical, stochastic approach.

Reed M Maxwell, Stefan J Kollet

August 24, 2007

Advances in Water Resources

## **Disclaimer**

---

This document was prepared as an account of work sponsored by an agency of the United States Government. Neither the United States Government nor the University of California nor any of their employees, makes any warranty, express or implied, or assumes any legal liability or responsibility for the accuracy, completeness, or usefulness of any information, apparatus, product, or process disclosed, or represents that its use would not infringe privately owned rights. Reference herein to any specific commercial product, process, or service by trade name, trademark, manufacturer, or otherwise, does not necessarily constitute or imply its endorsement, recommendation, or favoring by the United States Government or the University of California. The views and opinions of authors expressed herein do not necessarily state or reflect those of the United States Government or the University of California, and shall not be used for advertising or product endorsement purposes.

1 **Quantifying the effects of three-dimensional subsurface heterogeneity on Hortonian runoff**  
2 **processes using a fully-coupled numerical, stochastic approach.**

3 Reed M. Maxwell and Stefan J. Kollet\*

4 *Atmospheric, Earth and Energy Sciences Department, Lawrence Livermore National*

5 *Laboratory, Livermore, CA, USA*

6 *\*Current Address: Meteorological Institute, Bonn University, Germany*

7

8 *Aug 23, 2007*

9

10 **Abstract**

11       The impact of three-dimensional subsurface heterogeneity on hillslope runoff generated  
12 by excess infiltration (so called Hortonian runoff) is examined. A fully-coupled, parallel  
13 subsurface overland flow model is used to simulate runoff from an idealized hillslope.  
14 Ensembles of correlated, Gaussian random fields of saturated hydraulic conductivity are used to  
15 create uncertainty and variability (i.e. structure) due to subsurface heterogeneity. A large  
16 number of cases are simulated in a parametric manner with variance of the hydraulic  
17 conductivity varied over two orders of magnitude. These cases include rainfall rates above,  
18 equal and below the geometric mean of the hydraulic conductivity distribution. These cases are  
19 also compared to theoretical considerations of runoff production based on simple assumptions  
20 regarding (1) the rainfall rate and the value of hydraulic conductivity in the surface cell using a  
21 spatially-indiscriminant approach; and (2) a percolation-theory type approach to incorporate so-  
22 called runoff. Simulations to test the ergodicity of hydraulic conductivity on hillslope runoff are  
23 also performed. Results show three-dimensional features (particularly in the vertical dimension)  
24 in the hydraulic conductivity distributions that create shallow perching, which has an important

25 effect on runoff behavior that is fundamentally different in character than previous two  
26 dimensional analyses. The simple theories are shown to be very poor predictors of the saturated  
27 area that might runoff due to excess infiltration. It is also shown that ergodicity is reached only  
28 for a large number of integral scales ( $\sim 30$ ) and not for cases where the rainfall rate is less than  
29 the geometric mean of the saturated hydraulic conductivity.

30

### 31 **Introduction and Background**

32 There has been interest and need to understand the role of the subsurface heterogeneity in  
33 the processes of overland flow runoff generation. Though the role of heterogeneity has been  
34 investigated in previous studies (e.g. Woolhiser et al, 1996), in the processes of runoff and re-  
35 infiltration of overland flow (so-called runon), the interactions between the uncertainty in spatial  
36 variability in saturated hydraulic conductivity,  $K_s$ , and the ensuing impact on runoff processes  
37 have not been greatly explored. Two recent papers by Nahar et al. (2004) and Herbst et al.  
38 (2006) have addressed these concepts and, in addition, comprehensively summarized the pre-  
39 existing literature. Therefore only studies dealing with coupled subsurface and overland flow  
40 using stochastic representations will be discussed here.

41 Perhaps the first study to look at coupled surface-subsurface flow utilizing a stochastic  
42 representation of  $K_s$  was Binley et al. (1989). They simulated three dimensional subsurface  
43 random fields of  $K_s$  using a correlated, Gaussian approach and demonstrated its impact on  
44 overland flow due to excess infiltration and excess saturation. They looked at different cases  
45 with different parameter vales but performed a limited number of simulations due to the  
46 computational constraints at that time.

47 Nahar et al (2004) used an overland flow formulation with an analytical, single-column  
48 subsurface infiltration model to investigate field-scale infiltration caused by runon (downslope

49 re-infiltration of runoff due to an increase in  $K_s$ ) using two dimensional, correlated random fields  
50 to simulate subsurface properties. They showed the importance of runoff on subsurface recharge.  
51 They also presented a non-dimensional framework and investigated the uncertainty in spatial  
52 distribution of  $K_s$  using a Monte Carlo approach for some cases over a modest range of  
53 parameter values. Using this approach they showed that for rainfall rates lower than the mean  
54 hydraulic conductivity outflow increases with increasing heterogeneity (increasing variance in  
55  $K_s$ ) but found this relationship reversed for greater rainfall rates.

56         Herbst et al (2006) applied a three dimensional hydrologic model to a small catchment.  
57 They looked at five different representations of subsurface heterogeneity and compared the  
58 hydrologic model results to the actual system. They found that a conditional stochastic approach  
59 best represented the conditions of the real system.

60         Though primarily focused on theoretical surface-subsurface coupled model development,  
61 Kollet and Maxwell (2006) investigated the effects of correlated, random fields of  $K_s$  on overland  
62 flow in a two-dimensional (vertical) test case. Using a small number of realizations this work  
63 showed how shallow perching, runoff, runoff and infiltration interact simultaneously to affect  
64 hillslope outflow.

65         These previous studies all point to the need for an investigation of these processes and  
66 their interactions in a more systematic manner. In the current study, we apply a novel, fully  
67 coupled surface-subsurface flow model to investigate the effects of three-dimensional  
68 heterogeneity in  $K_s$  on overland flow using a comprehensive set of simulations. These  
69 simulations are designed to address the following four questions:

- 70             1. How does three-dimensional subsurface heterogeneity influence (transient)  
71                 outflow rates and their variability?

- 72           2. What is the fraction of saturated area for a certain rainfall rate and can we use  
73           estimates of this fraction to deduce average outflow rates (or vice versa)?  
74           3. Does a two-dimensional representation of subsurface heterogeneity suffice or is a  
75           three-dimensional representation necessary to capture accurately runoff  
76           processes?  
77           4. Does the concept of ergodicity apply? That is, how large does a hillslope have to  
78           be, with regard to the scale of the heterogeneity, to exhibit effective behavior?

79           In order to address these questions, we perform a large number of numerical experiments.  
80           These experiments include a wide range of parameter values with a variance of  $K_s$  spanning two  
81           orders of magnitude. Additionally, we simulate three dimensional structure in the subsurface  
82           heterogeneity and ergodic domains, both features not previously investigated. First, the coupled  
83           modeling approach is presented; next, non-dimensional parameters are introduced; and third, the  
84           case studies, including a table of parameter values, are detailed. Finally, the results of the  
85           simulations are presented and discussed along with implications for field scale runoff.

86

## 87 **Coupled Model**

88           In this study, we use the flow code ParFlow to simulate fully-coupled surface and  
89           subsurface flow via an overland flow boundary condition. While complete details of this  
90           approach are given in Kollet and Maxwell (2006), a brief summary of the equations are  
91           presented below. ParFlow solves the Richards' equation in three spatial dimensions which may  
92           be written as:

93           
$$S_s S_w \frac{\partial \psi_p}{\partial t} + \phi \frac{\partial S_w(\psi_p)}{\partial t} = \nabla \cdot \mathbf{q} + q_s \quad (1)$$

94  $q = -K_s(x)k_r(\psi_p)\nabla(\psi_p - z)$

95 where  $\psi_p$  is the subsurface pressure head [L],  $z$  is depth below the surface [L],  $K_s(x)$  is the  
 96 saturated hydraulic conductivity [ $LT^{-1}$ ],  $k_r$  is the relative permeability [-] (a function of pressure  
 97 head,  $\psi_p$ ),  $S_s$  is the specific storage coefficient [ $L^{-1}$ ],  $\phi$  is the porosity [-],  $S_w$  is the degree of  
 98 saturation [-] and  $q_s$  is the general source/sink term [ $T^{-1}$ ].

99 Shallow overland flow is represented in ParFlow by the two-dimensional kinematic wave  
 100 equation, which appears in the overland flow boundary condition after applying continuity  
 101 conditions of pressure and flux:

102 
$$-K_s(x)k_r(h-z) = \frac{\partial \|h_s, 0\|}{\partial t} - \nabla \bar{v} \|h_s, 0\| + q_r(x) \quad (2)$$

103 where  $\bar{v}$  is the depth averaged velocity vector [ $LT^{-1}$ ];  $h_s$  is the surface ponding depth [L] and  
 104  $q_r(x)$  is the a general source/sink (e.g. rainfall) rate [ $LT^{-1}$ ]. Note that  $\|h_s, 0\|$  indicates the greater  
 105 value of the two quantities and that the overland flow condition assumes that  $h_s = \psi_p$  at the ground  
 106 surface under saturated conditions (Kollet and Maxwell, 2006). If diffusion terms are neglected  
 107 the momentum equation can be written as

108 
$$S_{f,i} = S_{o,i} \quad (3)$$

109 which is commonly referred to as the kinematic wave approximation. In Equation 3  $S_{o,i}$  is the  
 110 bed slope (gravity forcing term) [-], which is equal to the friction slope  $S_{f,i}$  [L];  $i$  stands for the  $x$ -  
 111 and  $y$ -direction.

112 Manning's equation is used to establish a flow depth-discharge relationship

113 
$$v_x = -\frac{\sqrt{S_{f,x}}}{n} h_s^{2/3} \quad \text{and} \quad v_y = \frac{\sqrt{S_{f,y}}}{n} h_s^{2/3} \quad (4)$$

114 where  $n$  [ $TL^{-1/3}$ ] is the Manning's coefficient.

115 ParFlow additionally has the ability to represent the hydraulic conductivity distribution of  
 116 the subsurface as a correlated, space random field using a parallel, Turning Bands approach  
 117 (Tompson et al 1989; Ashby and Falgout, 1996; Tompson et al 1998). To incorporate this  
 118 feature, we choose to represent the spatial variation of hydraulic conductivity as a statistically  
 119 stationary, random field where:

$$120 \quad \ln K(\mathbf{x}) = F + f(\mathbf{x}) \quad (5)$$

121 and  $\overline{\ln K(x)} = F$ ,  $\overline{f(x)} = 0$  with  $\overline{f(x)^2} = \sigma_f^2 = \sigma_{\ln K}^2$  and  $K_g = e^F$ . The mean or expected value  
 122 of the  $\ln K$  is signified by the overbar and  $K_G$  is the geometric mean of the hydraulic conductivity.  
 123 The correlation of any two hydraulic conductivity values separated by a distance,  $\xi$ , with a  
 124 correlation scale,  $\lambda$ , is represented by an exponential of the form:

$$125 \quad R_{ff}^e(\xi) = \sigma_f^2 e^{-\xi/\lambda} \quad (6).$$

126 Note that the correlation scale,  $\lambda$ , in (6) is equivalent to the integral scale,  $I$  (see section  
 127 2.3.1 in Rubin, 2003). While this technique of representing spatially correlated heterogeneity  
 128 has been widely applied in subsurface flow (e.g., Smith and Schwartz, 1980; Dagan, 1989;  
 129 Tompson and Gelhar, 1990; Rubin and Dagan, 1992) it is an approximate description of the  
 130 subsurface heterogeneity usually applied at smaller spatial scales (e.g. Carle and Fogg, 1996;  
 131 Carle and Fogg, 1997; Tompson et al, 1998).

132

### 133 **Non-dimensionalization of the governing equations.**

134 First, we introduce the rain application time,  $t_a$  and the length of the hillslope,  $L$ , in the  
 135 direction of overland flow. We are interested in the relationship between the rainfall rate and the  
 136 ability of the subsurface to infiltrate this rainfall. It is common to think about the rainfall rate,  
 137  $Q_{rain}$ , in relation to the saturated hydraulic conductivity of the subsurface,  $K_s$ . However, we are



138 using a correlated, space-random field to simulate the subsurface heterogeneity in  $K_s$ , therefore  
 139 we choose to non-dimensionalize  $Q_{rain}$  by the geometric mean of the hydraulic conductivity

$$140 \quad q_r' = \frac{Q_{rain}}{K_g} \quad (7).$$

141 It is then natural to transform saturated hydraulic conductivity in the same manner, as

$$142 \quad K' = \frac{K_s}{K_g} \quad (8).$$

143 We may then combine saturation and porosity:

$$144 \quad S' = \phi S \quad (9).$$

145 As we are interested in non-dimensionalizing with respect to the length scales of heterogeneity,  
 146 we define  $L$  in terms of integral scales,  $I_x=I_y$ :

$$147 \quad x' = \frac{x}{L} = \frac{x}{I_{x,y}} \quad (10), \text{ and}$$

$$148 \quad z' = \frac{z}{L} = \frac{z}{I_{x,y}} \quad (11).$$

149 As stated earlier, we define time in terms of application time of the rainfall,  $t_a$ :

$$150 \quad t' = \frac{t}{t_a} \quad (12).$$

151 This results in the following parameter groupings for the soil pressure head and ponding depth:

$$152 \quad h' = \frac{h}{K_g t_a} \quad (13),$$

153 and the velocity:

$$154 \quad v' = \frac{v t_a}{L} = \frac{v t_a}{I_{x,y}} \quad (14).$$

155 The governing equations, then become:

156 
$$\frac{\partial S'}{\partial t'} = \nabla \cdot [k' k_r \nabla (h' - z')] \quad (15)$$

157 
$$-k' k_r \nabla (h' - z') = \frac{\partial \|h', 0\|}{\partial t'} - \nabla v \|h', 0\| - q'_r \quad (16).$$

158

159 **Problem Setup**

160 To investigate the effects of three-dimensional subsurface heterogeneity on Hortonian  
 161 hillslope runoff, we employ the numerical experiment shown in Figure 1. The experiment  
 162 consists of a uniform hillslope that terminates at a perpendicular channel. Water may exit the  
 163 hillslope anywhere along the channel though flow in the channel is not explicitly simulated. The  
 164 domain size is 6x6 integral scales and the lateral grid dimensions are  $n_x=n_y=30$  and  $\Delta x'=\Delta y'=0.2$   
 165  $I_{x,y}$ . We use a fine vertical discretization with  $n_z=150$  (for 135,000 compute cells) and  $\Delta z' =$   
 166  $0.0004 I_{x,y}$ , (or  $0.04 I_z$ ) for a default domain size  $6 I_z$  deep, to insure accurate solutions of surface-  
 167 subsurface interactions. The friction slopes are constant in the  $x$ - and  $y$ -direction  $S_{fx}=0$ ,  $S_{fy}=-$   
 168  $0.005$  with a constant manning's roughness coefficient of  $2.9 \times 10^{-6} (t_d/I_{x,y})^{1/3}$ . Rain is applied  
 169 uniformly over the entire hillslope for  $\Delta t'=1$  with an ensuing recession of an additional  $\Delta t'=1$   
 170 resulting in a total simulation time of  $t'=2$ . To ensure Hortonian conditions, the water table is  
 171 initialized at the bottom of the domain resulting in an initial hydrostatic pressure distribution  
 172 with dry conditions at the ground surface.

173 The numerical experiments are designed to directly address the four questions posed  
 174 earlier. For the complete set of numerical experiments, we systematically change the variance of  
 175 the hydraulic conductivity field,  $\sigma_{\ln K}^2$ , (i.e. the degree of subsurface heterogeneity), the  
 176 normalized rainfall rate, the statistical anisotropy and the size of the domain.

177 For the base-case, we performed a series of simulations using statistically anisotropic  
178 fields with  $\varepsilon=I_z/I_{x,y}=0.01$  (as defined in Rubin, 2003 and Dagan, 1989). The results of these  
179 simulations are used to quantify the influence of subsurface heterogeneity on outflow rates and to  
180 study the relationship of fraction of saturated area and outflow rate. Additionally, statistically  
181 isotropic simulations were performed and compared to the anisotropic simulations to examine  
182 whether a two-dimensional representation of subsurface heterogeneity suffices to capture the  
183 main processes of runoff production. We simulate 50 realizations of hydraulic conductivity  
184 distribution for each case and average all results over this ensemble. Each realization was  
185 generated using a parallel version of the turning bands algorithm (Tompson et al, 1989) utilizing  
186 75 lines,  $r_\zeta=5.0$  and  $\Delta k=0.2$ .

187 Additionally, we simulated six ergodic cases that are  $72I_x$  wide consisting of a single  
188 realization. Again, we use a parallel version of the turning bands algorithm utilizing 350 lines,  
189  $r_\zeta=5.0$  and  $\Delta k=0.2$ . This set of simulations examines the average behavior of a hillslope, which  
190 is of great significance with regard to upscaling. In summary, we simulate 33 different cases  
191 including 1,209 different individual simulations. All simulations and associated parameters are  
192 shown in Table 1.

193 Figure 2 displays the five lognormal distributions of hydraulic conductivity used in these  
194 numerical simulations, normalized by the rainfall rate. This figure also delineates the three non-  
195 dimensional rainfall rates used in this study. Inspection of this figure provides some indication  
196 of expected runoff behavior; for example, simulations using the intermediate rainfall rate should  
197 show very little sensitivity to  $\sigma_{\ln K}^2$ .

198  
199  
200

201 Table 1. List of all numerical simulations and parameter values.

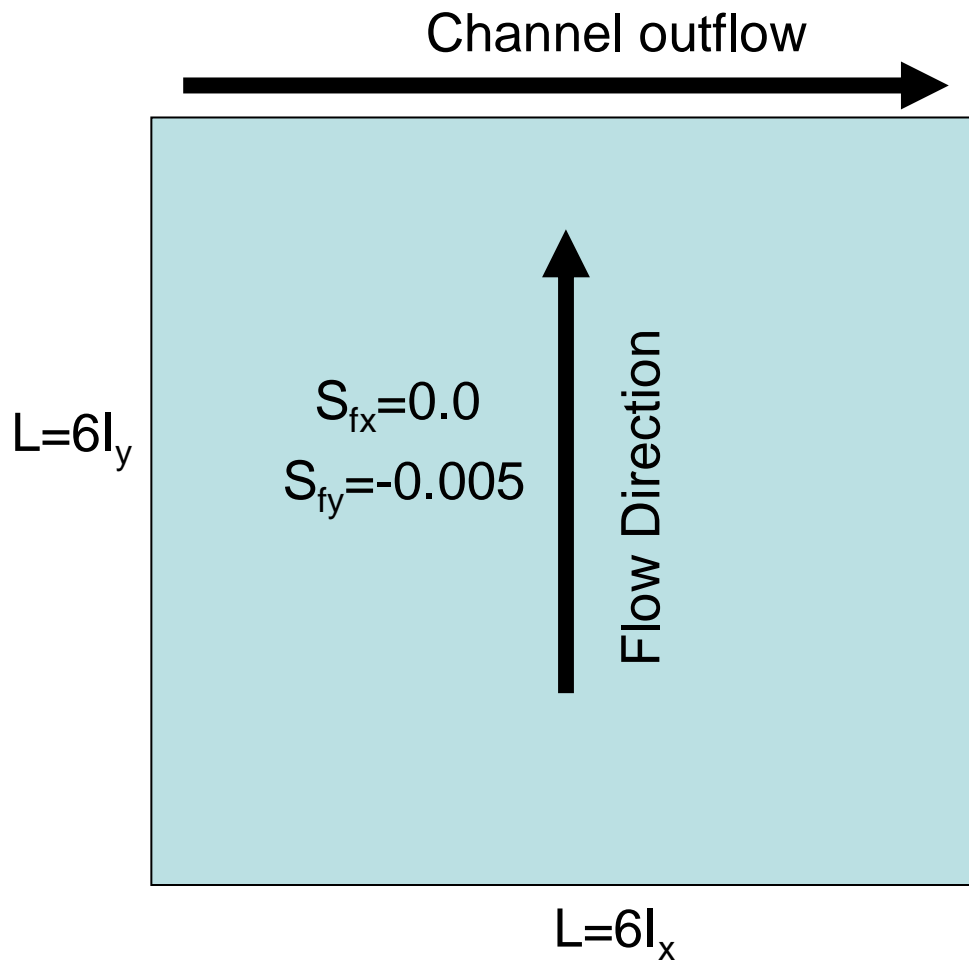
Simulations	$\sigma_{\ln K}^2$	$Q_{rain}/K_g$	$\varepsilon$	$L_x$	Number of realizations
Anisotropic (base case)	0.1	0.5	0.01	6	50
	0.5				
	1				
	5				
	10				
	0.1	1.0			
	0.5				
	1				
	5				
	10				
	0.1	2			
	0.5				
	1				
	5				
	10				
Isotropic	1	0.5	1		
	0.5				
	5				
	1	1.0			
	0.5				
	5				
	1	2			
	0.5				
	5				
Ergodic	0.5	1	0.1	72	1
	1.0				
	5				
	0.5	0.5			
	1.0				
	5				
	0.5	2			
	1.0				
	5				

202

203

204

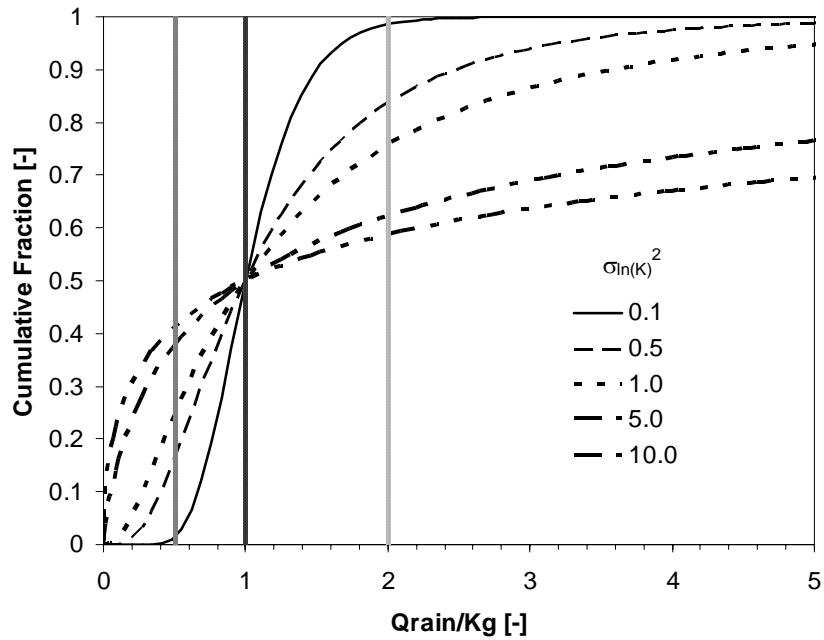
205



206

207

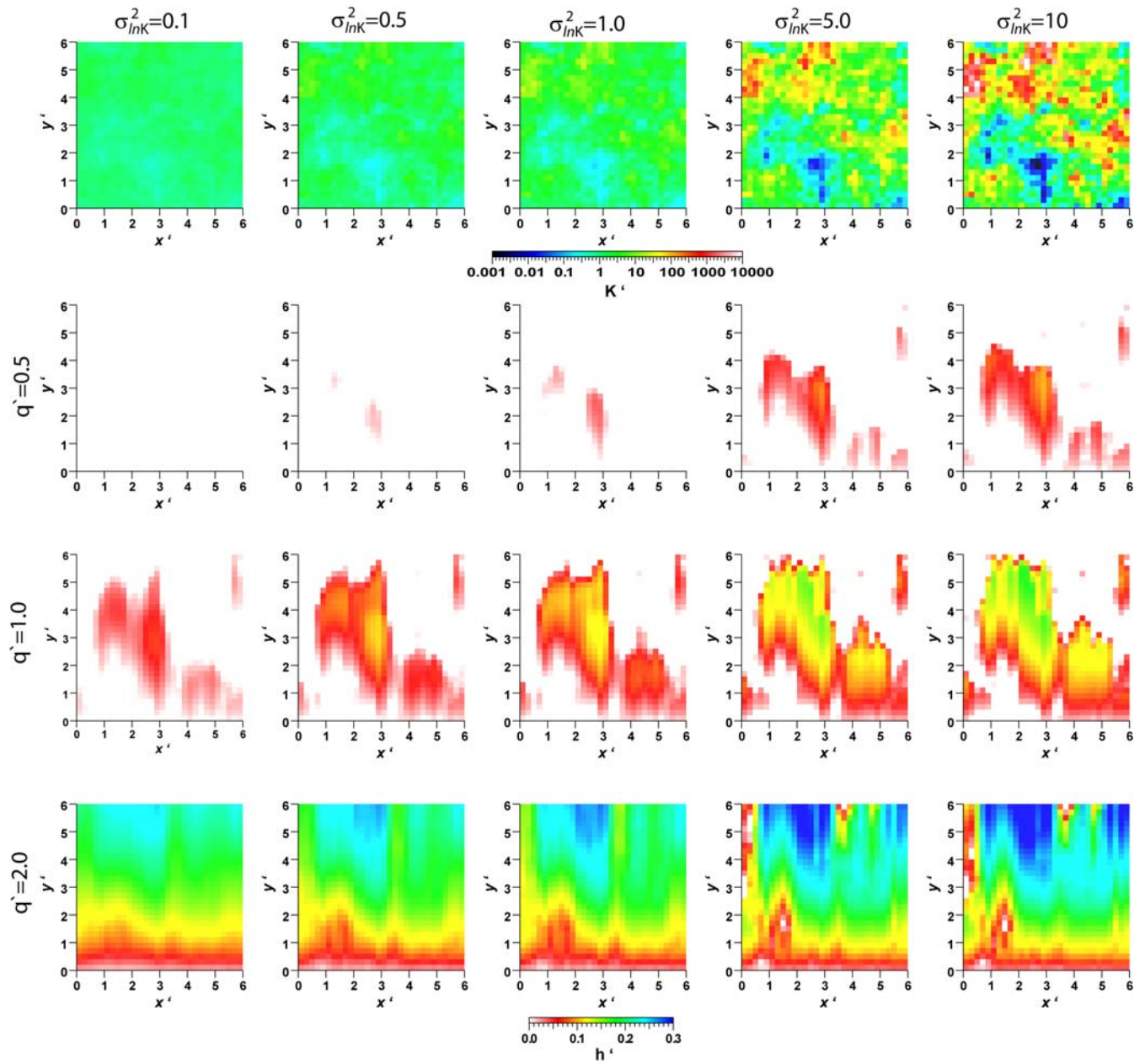
Figure 1. Problem setup and schematic.



208

209 Figure 2. Plot of cumulative, lognormal distributions for the five variances used in this study, normalized as a  
 210 function of rainfall rate over the geometric mean of hydraulic conductivity. The three normalized rainfall rates are  
 211 also plotted on this figure as gray, vertical lines.

212



213

214 Figure 3. Plot of non-dimensional hydraulic conductivity ( $K'$ ) at the land surface (top) for a range of increasing

215 variances of  $\ln K$  from left to right as shown for a single realization, 20. Next three rows are plots of non-

216 dimensional depth of ponded water ( $h'$ ) for these corresponding realizations at  $t'=1$  for increasing non-dimensional

217 rainfall rates  $q'=0.5, 1.0$  and  $2.0$ . Note outflow occurs at the top of each panel.

218

219

220

221 **Results and Discussion**

222 Figure 3 plots a single realization of hydraulic conductivity field for the range of  $\sigma_{\ln K}^2$   
223 simulated in this work. All plots are for the same random seed (and thus the same spatial pattern  
224 of heterogeneity), with  $\sigma_{\ln K}^2$  increasing from left to right. Also shown in the figure are the  
225 corresponding depths of ponded water at  $t^*=1$ , the time of peak flow. These plots are for cases of  
226 increasing  $Q_{rain}$  from top to bottom. These plots illustrate the increase in ponding depth both  
227 with increasing rainfall (top to bottom Figure 3) and increasing heterogeneity (left to right,  
228 Figure 3).

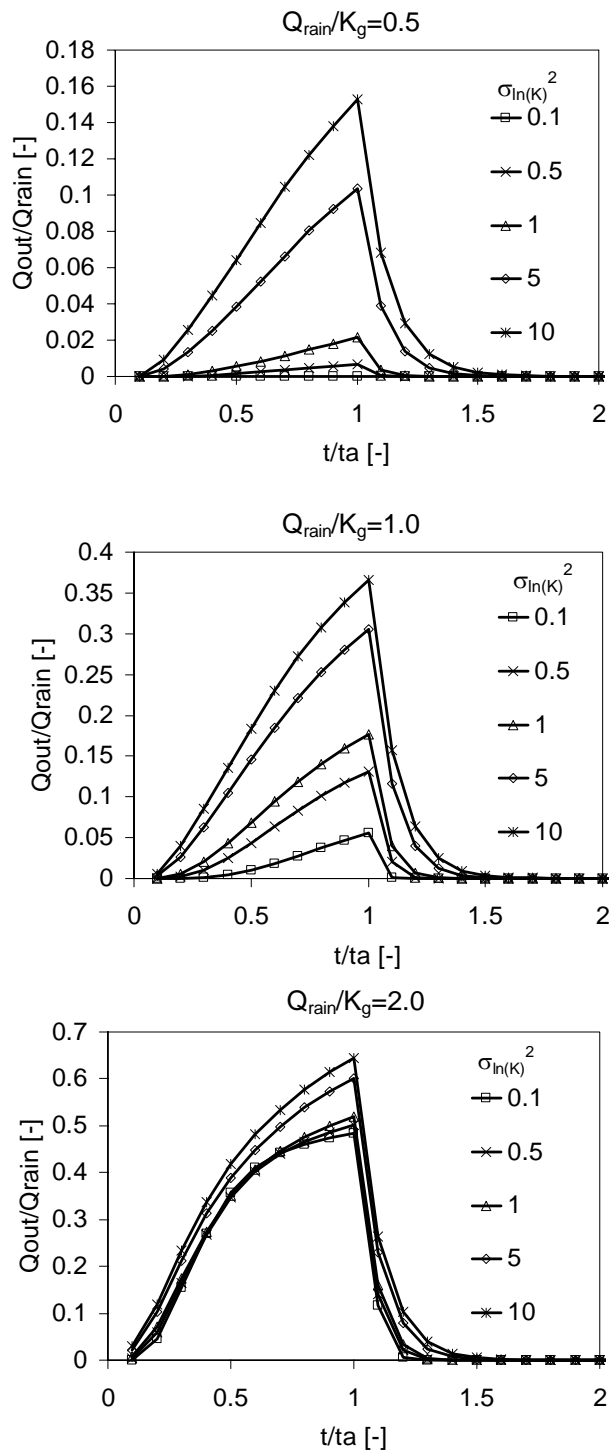
229 Figure 4 plots the non-dimensional hydrograph, averaged over all realizations for the  
230 base-case simulations; that is for five  $\sigma_{\ln K}^2$  and three non-dimensional rainfall rates. In this figure  
231 we see an increase in outflow with increasing  $\sigma_{\ln K}^2$  for all three rainfall rates. This increase is  
232 most significant for the lowest rainfall rate and least significant for the highest rainfall rate.

233 Figure 5 summarizes this information, plotting the total, non-dimensional outflow as a  
234 function of  $\sigma_{\ln K}^2$  for the three rainfall rates. This figure plots the ensemble average outflow over  
235 all realizations (solid line) and the average +/- one standard deviation of outflow (dashed lines).  
236 In this figure, we again see an increase in percent total outflow with increasing  $\sigma_{\ln K}^2$ . There is  
237 also an increasing variance in the outflow rate (generated by the difference in outflow from  
238 different realizations of hydraulic conductivity) with increasing  $\sigma_{\ln K}^2$ .

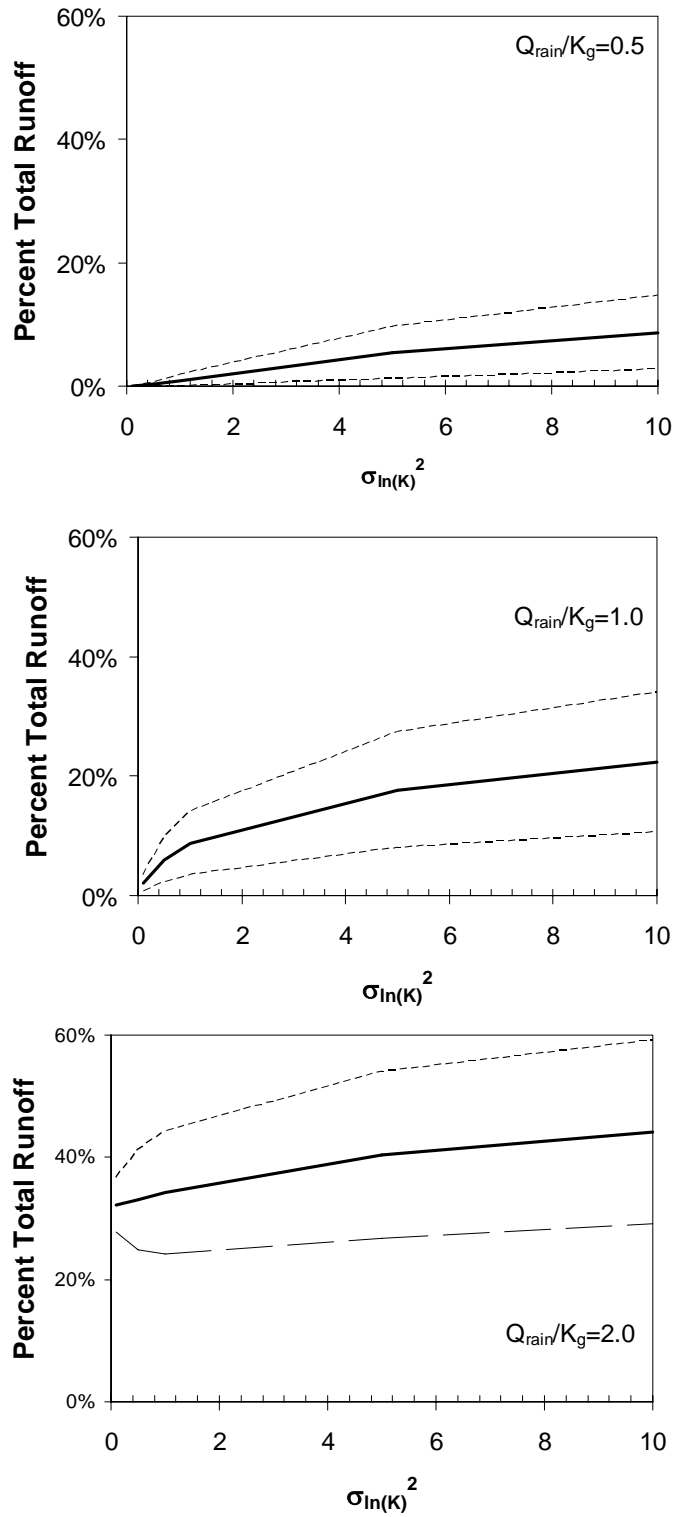
239

240





241  
 242 Figure 4. Plot of the ensemble average of non-dimensional outflow against non-dimensional time for five values of  
 243 variance of  $\ln(K)$  (different symbols as noted) for three non-dimensional rainfall rates, as labeled, increasing in  
 244 amount from the top panel to the bottom panel. Note the different scale for the y-axis in the three panels of this  
 245 figure.



246

247 Figure 5. Plot of percent total runoff as a function of variance of  $\ln(K)$  for the three non-dimensional rainfall rates

248 simulated. The average over all realizations is plotted as the solid line while the average  $\pm$  one standard deviation

249 is plotted as the dashed lines.

250

251 At the ground surface, the fractional saturated area (cells with  $S_w \geq 1$  and  $\psi \geq 0$ ) was  
252 calculated at  $t^*=1$  (time of peak flow) for all  $\sigma_{\ln K}^2$  values and rainfall rates in two distinct ways.  
253 First, the fractional area was calculated, regardless of connection to the channel, i.e. any  
254 saturated area was counted regardless of spatial orientation. In the second approach, only those  
255 cells were counted that provided a contiguous or connected saturated path to the channel. The  
256 calculated fractional saturated areas were then averaged over all realizations. Figure 6 plots the  
257 results of this calculation, fraction of saturated area, total and connected, as a function of  $\sigma_{\ln K}^2$   
258 for the three rainfall rates. In this figure we see that for the lowest rainfall rate ( $Q_{rain}/K_g=0.5$ , left  
259 panel) the fraction of saturated area increases with increasing  $\sigma_{\ln K}^2$ . This is also the case for the  
260  $Q_{rain}/K_g=1.0$  case (middle panel) though there is less of an increase for larger  $\sigma_{\ln K}^2$ . For the  
261 largest rainfall rate ( $Q_{rain}/K_g=2.0$ ) we see the opposite relationship; decreasing fractional  
262 saturated area with increasing  $\sigma_{\ln K}^2$ .

263 In Hortonian overland flow, one may attempt to calculate the fraction of ponded, or  
264 saturated surface cells based on the shape of the assumed distribution of  $\ln(K)$  and the rainfall  
265 rate. This may be done in two ways, one that does not take into account the lateral spatial  
266 structure of the saturated hydraulic conductivity field and one that does and accounts for both  
267 runoff and runoff processes. For the former case, the fraction of saturated area may be calculated  
268 as the fraction of the distribution of  $\ln(K)$  that is less than the rainfall rate. This may be viewed  
269 graphically as the intersection of the rainfall values and the distribution of  $\ln(K)$  shown in Figure  
270 2. This approach is similar in concept to runoff parameterizations in many classes of land  
271 surface models (e.g. Wetzel et al, 1996; Liang et al, 1996; Lohmann et al, 1998). For the latter,  
272 connected case, the lateral spatial distribution saturated hydraulic conductivity affects the

273 calculation. In this case, the fraction of saturated hydraulic conductivity values below the  
274 rainfall rate, connected to the channel (starting at the outflow side of the hillslope and working  
275 upward) were calculated from the generated random fields and then averaged. These calculations  
276 were performed for both cases are plotted as a function of rainfall rate and variance as the heavy  
277 solid (total) and dashed lines (connected) in Figure 6.

278 We see, in Figure 6, that the fractional surface saturated areas calculated from the  
279 distributions of hydraulic conductivity almost always under-predict the simulated values. Only  
280 at the smallest variance of 0.1 do the fractional surface saturations agree and the most  
281 pronounced differences are for values of  $\sigma_{\ln K}^2$  greater than one. The largest difference (50%) in  
282 the predicted and simulated fractional saturated surface area is for the rainfall rate of  
283  $Q_{rain}/K_g=1.0$ . At this rainfall value, the fractional surface areas calculated from the distribution  
284 of  $\ln(K)$  predict no change with variance of  $\ln(K)$ . The simulated values show that this not the  
285 case and suggest that consideration of other processes is important, which are discussed below.

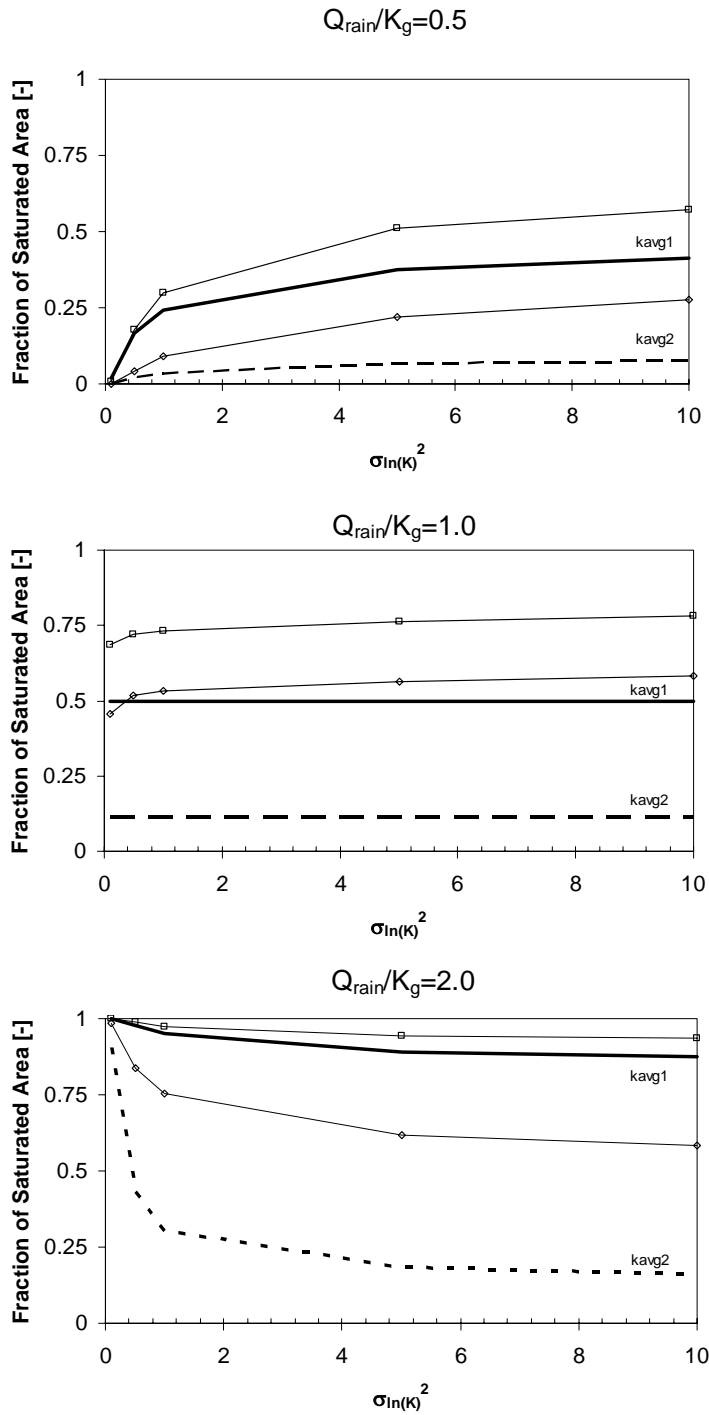
286 There are two physical processes accounted for in the simulations that create the  
287 differences seen in Figure 6. These processes are runoff-generated excess infiltration and  
288 shallow perched or ponded zones. Runoff generated excess infiltration occurs when the saturated  
289 hydraulic conductivity of a tile is greater than the rainfall rate but not greater than the sum of the  
290 rainfall rate and the inflow from an upslope tile that is already saturated and generating runoff.  
291 This is a variation of the runoff process but instead of the runoff water leading to subsurface  
292 infiltration as simulated by previous studies, it may still run off later from a downslope tile, given  
293 these conditions.

294 Shallow perching is ponded water that builds up at the land surface (and runs off) not due  
295 to the surface value of hydraulic conductivity being lower than the rainfall rate but due to low- $K$   
296 values just below the land surface. This water initially infiltrates but eventually cannot flow past

297 a low- $K$  layer in the shallow subsurface and saturates the cells above this low- $K$  cell and  
298 eventually ponds water at the land surface which then runs off. An example of this phenomenon,  
299 as simulated by the coupled model, may be seen in Figure 13 of Kollet and Maxwell (2006). It is  
300 clear from Figure 6 that both these processes are occurring and important, particularly at large

301  $\sigma_{\ln K}^2$ .

302



303

304

Figure 6. Plot of calculated fractional total (thin lines with squares) and connected (thin lines with diamonds)

305

saturated area at  $t' = 1$ , averaged over all realizations, as a function of variance of  $ln(K)$  for the three rainfall rates.

306

The fractional areas predicted by the distribution of hydraulic conductivity that is less than the rainfall rate is also

307

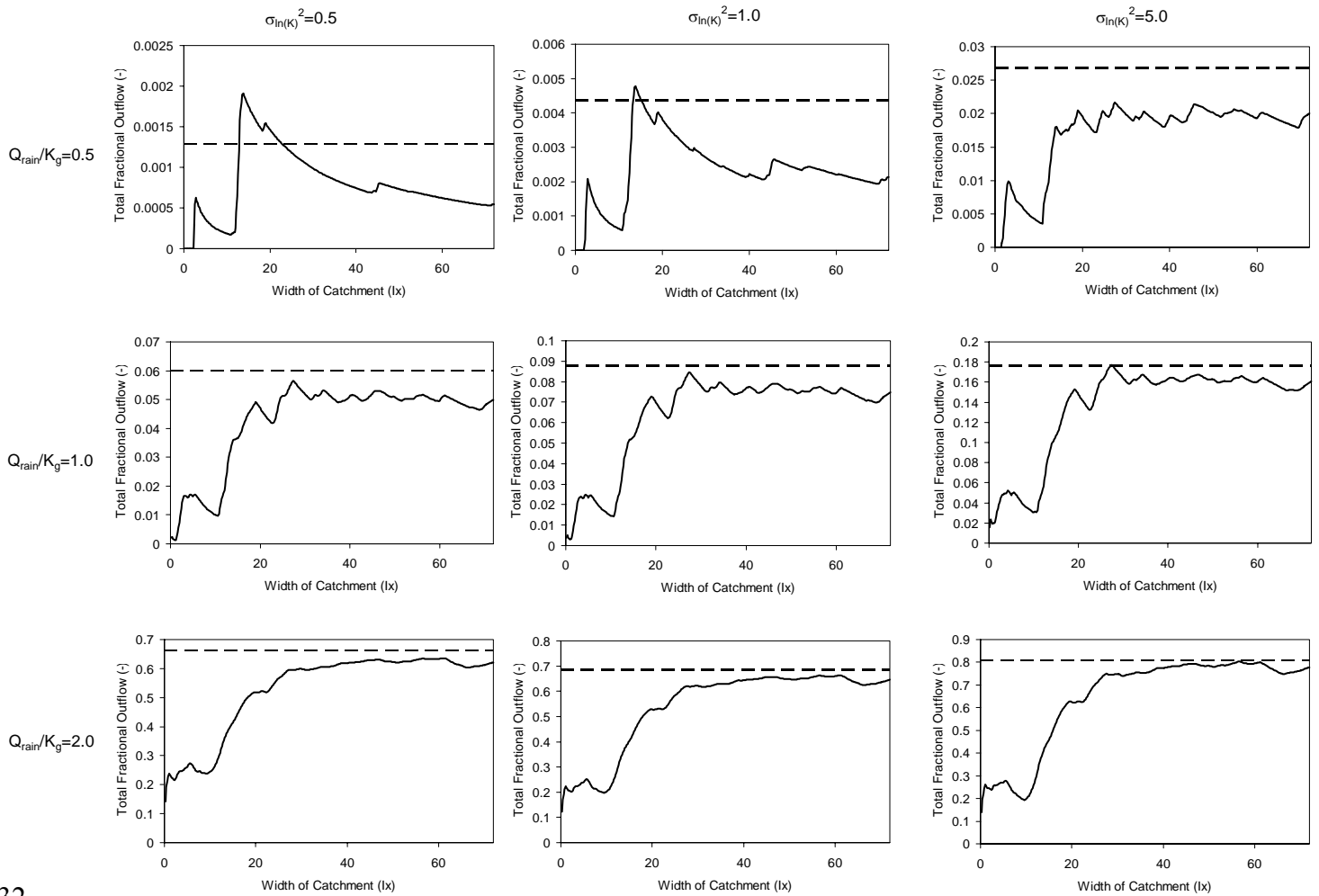
shown for total ( $k_{avg1}$ , heavy solid line) and connected ( $k_{avg2}$ , dashed line).

308

309           The ergodicity of heterogeneous hillslope processes have not been previously  
310 investigated. Ergodicity has, however, been a common topic in other areas such as subsurface  
311 transport (e.g. Dagan, 1989; Rubin, 2003) and is defined as the equivalence between spatial and  
312 ensemble statistics (Rubin, 2003). The condition of ergodicity plays an important role in  
313 understanding when a hillslope is of sufficient spatial scale that effective behavior would be  
314 expected. Therefore, understanding of ergodicity is key in upscaling subgrid heterogeneity to  
315 simulate runoff processes in large scale models.

316           In order to examine ergodicity, a series of very large (72 Integral scales wide) domains  
317 were constructed for three  $\sigma_{\ln K}^2$  values, 0.5, 1.0 and 5.0, for the three rainfall rates. The  
318 cumulative outflow was calculated and normalized for increasing distances (and thus  
319 corresponding hillslope areas) along the channel (i.e. the  $x$ -axis). In this way, not only the total  
320 fractional outflow, but the fractional outflows for domain widths ranging from 0.2 to  $72I_x$  could  
321 be calculated as well. These outflows are plotted in Figure 7 as a function of non-dimensional  
322 catchment width for the three values of  $\sigma_{\ln K}^2$  and for the three rainfall rates (solid curves). For  
323 each plot, the corresponding ensemble average of total fractional outflow was also plotted  
324 (dashed curves). Comparison of these two curves (and particularly their intersection) provides  
325 an estimate of the catchment width needed for ergodic behavior of Hortonian runoff.

326           Inspection of the curves in Figure 7 demonstrates several important features. One, the  
327 total outflow again increases both with increasing  $\sigma_{\ln K}^2$  and with increasing rainfall rate.  
328 Additionally, for lower variances ( $\sigma_{\ln K}^2=0.5$  and 1.0) and for the lowest rainfall rate, ergodic  
329 behavior with catchments narrower than  $72I_x$  is unlikely. For the two larger rainfall rates,  
330 ergodic behavior is approached at catchments approximately 30 integral scales wide with a  
331 smoother transition to ergodic behavior at the largest rainfall rate.



332

333 Figure 7. Plot of total fractional outflow as a function of increasing catchment width for a large, single realization of  
 334 hydraulic conductivity (solid line), for three variances of  $\ln(K)$  (left to right) and for increasing non-dimensional  
 335 rainfall rate (top to bottom). The ensemble average of total fractional outflow (as in Figure 5) is plotted as the  
 336 horizontal, dashed line. Note the different y-axis for each panel in this figure.

337

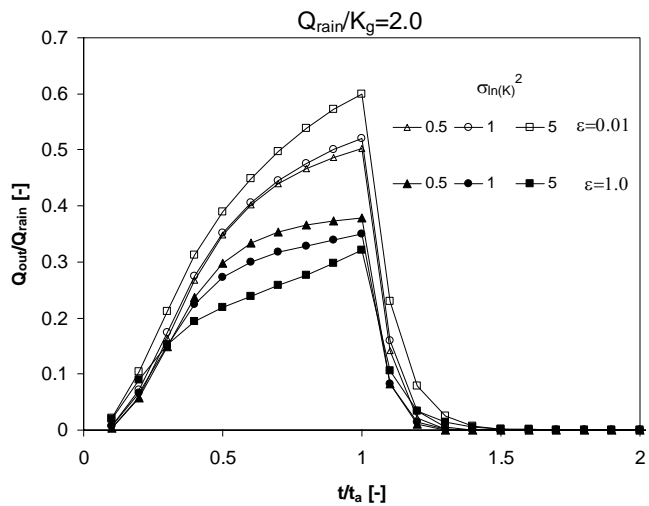
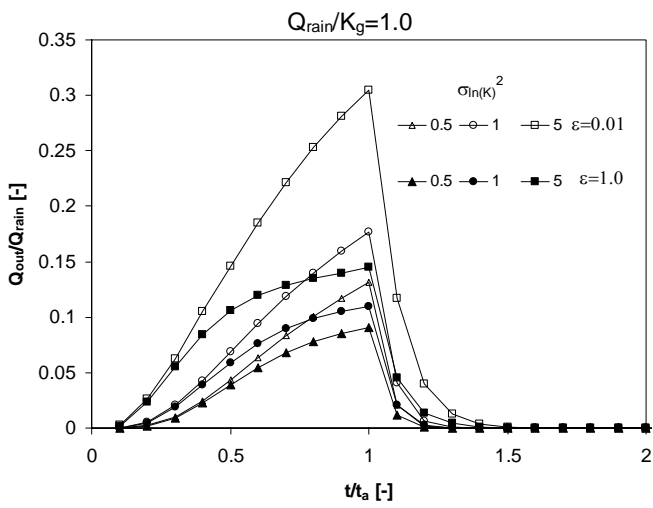
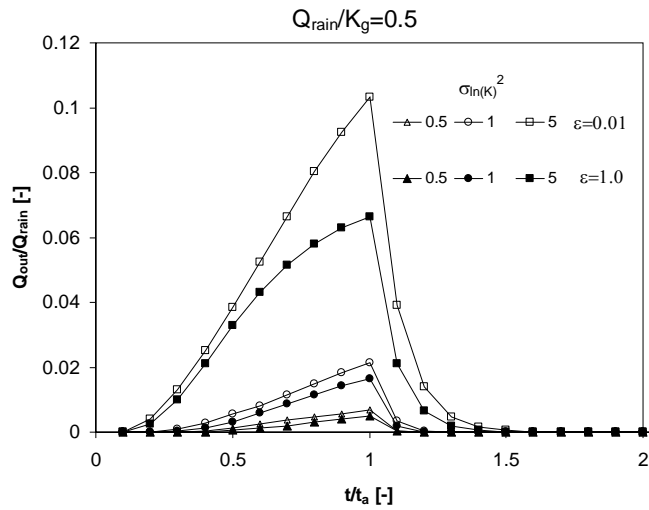
338 The trends seen in Figures 4 and 5 that outflow always increases with increasing  $\sigma_{\ln K}^2$ , are  
 339 somewhat counterintuitive, particularly at the larger rainfall rates. Additionally, these trends do  
 340 not agree with the findings of Nahar et al (2004). The work of Nahar and colleagues was more  
 341 simplified than the current study and among other aspects, only considered two-dimensional  
 342 random fields of hydraulic conductivity and did not fully couple the surface and subsurface in



343 the same manner done in the current work. Though they include the important process of runoff  
344 in their analysis, their results do not honor processes related to runoff-generated excess  
345 infiltration and additional processes resulting from vertical heterogeneity in the hydraulic  
346 conductivity, such as perching in the shallow subsurface. To investigate the importance of  
347 vertical structure in hydraulic conductivity and processes related to shallow perching a series of  
348 simulations with a much larger statistical anisotropy ratio,  $\varepsilon=1$ , were simulated and compared to  
349 the base-case simulations with  $\varepsilon=0.01$  for  $\sigma_{\ln K}^2 = 0.5, 1.0$  and  $5.0$ . Though still generated with a  
350 three-dimensional hydraulic conductivity field, with a vertical correlation length more than 16  
351 times larger than the thickness of the domain, these simulations are effectively two-dimensional.

352 The results of these simulations are plotted in Figures 8 and 9. Figure 8 plots non-  
353 dimensional outflow as a function of non-dimensional time for the three variances (lines with  
354 filled symbols) for the three rainfall rates (increasing from the top to bottom) averaged over all  
355 50 realizations. Also plotted are the corresponding base-case simulations with  $\varepsilon=0.01$  (curves  
356 with open symbols), the same curves shown in Figure 4. At the lowest rainfall rate (left panel)  
357 both sets of simulations show a trend of increasing outflow with increasing  $\sigma_{\ln K}^2$ . The  
358 statistically-anisotropic, base-case simulations predict more outflow than the statistically-  
359 isotropic simulations, particularly at  $\sigma_{\ln K}^2=5.0$ . At the intermediate rainfall rate,  $Q_{\text{rain}}/K_g=1.0$ , there  
360 still is a trend of increasing outflow with increasing  $\sigma_{\ln K}^2$ , but with a much larger difference  
361 between the statistically isotropic and anisotropic simulations in both the shape of the  
362 hydrograph and the total flow. At the largest rainfall rate, a reversal in trend between the  
363 statistically isotropic and anisotropic cases is observed. The base-case, with  $\varepsilon=0.01$  predicts an  
364 increasing runoff rate with increasing variance, while the statistically-isotropic case, with  $\varepsilon=1.0$ ,  
365 predicts the opposite behavior- decreasing outflow with increasing  $\sigma_{\ln K}^2$ .

366 Figure 9 confirms this behavior, plotting the percent total runoff as a function of variance  
367 of  $\ln(K)$  for the average of both cases (solid line) +/- one standard deviation (thin lines) with the  
368  $\epsilon=1.0$  case plotted with symbols. This figure also shows that the variance of the outflow behaves  
369 differently for the two cases, particularly at the largest rainfall rate. In this figure we see that the  
370 statistically anisotropic (i.e. 3D) cases produce greater runoff than the corresponding statistically  
371 anisotropic (i.e. 2D) cases. These differences are quite significant at the greatest values of  $\sigma_{\ln K}^2$   
372 and for the largest rainfall rates. These differences underscore the contribution of processes such  
373 as runoff-generated excess infiltration and shallow perching. Exclusion of these important  
374 processes could lead to significant errors in runoff estimation.



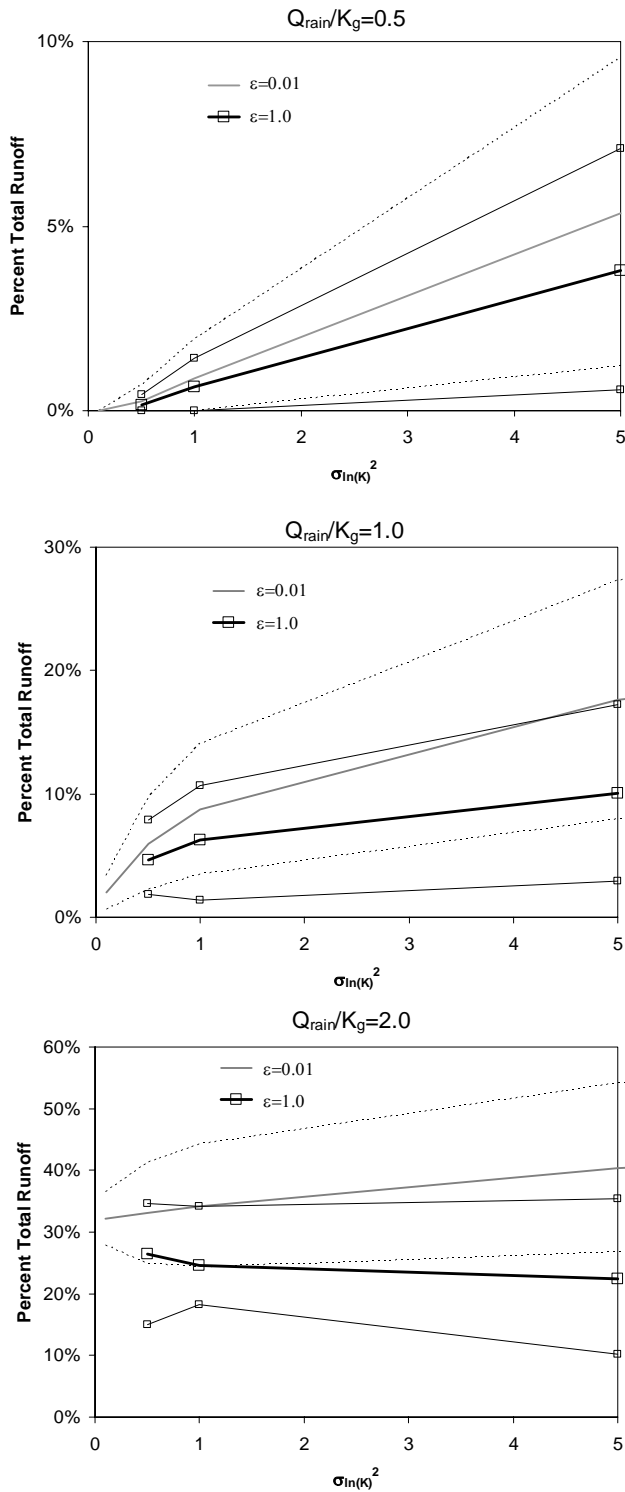
375

376

377

378

Figure 8. Plot of non-dimensional, ensemble-averaged outflow as a function of non-dimensional time for three variances (symbols as noted) for three non-dimensional rainfall rates (0.5, top to 2.0, bottom) for statistically isotropic ( $\epsilon=1.0$ ) and anisotropic ( $\epsilon=0.01$ ) cases. Note the difference in scale for the x-axis for the three figures.



379

380 Figure 9. Plot of percent total runoff, averaged over all realizations (heavy lines) and +/- one standard deviation  
 381 (thin lines), as a function of variance of  $\ln(K)$  for the statistically isotropic ( $\epsilon=1.0$ , symbols) and anisotropic ( $\epsilon=0.01$ ,  
 382 solid lines). Note the difference in scale for the x-axis for the three figures.

## 383 **Conclusions**

384 We applied a fully coupled subsurface, overland flow model to examine Hortonian runoff  
385 in a simple hillslope with a heterogeneous subsurface. We investigate parametrically, the effects  
386 of a wide range of variance of  $\ln K$ , normalized rainfall rates and statistical anisotropy. We also  
387 investigate ergodicity with several, very large domains, but only a single realization of hydraulic  
388 conductivity. Finally, we compare results of saturated area to some simple analytical tools for  
389 predicting excess infiltration areas. From these numerical experiments, we reach the following  
390 conclusions:

- 391 1. Three-dimensional subsurface heterogeneity, particularly vertical, structure in  $K_s$ , has a  
392 pronounced effect on Hortonian hillslope runoff. Statistical anisotropy in hydraulic  
393 conductivity produces trends in outflow with increasing  $\sigma_{\ln K}^2$  that are the opposite of a  
394 statistically isotropic subsurface. Additionally, the runoff produced from the statistically  
395 isotropic cases was greater than the runoff produced from the corresponding isotropic  
396 cases.
- 397 2. Runoff/infiltration percentage varies greatly with rainfall rate and variance of  $\ln(K)$ , i.e.  
398 degree of heterogeneity.
- 399 3. An ergodic limit was determined to be around 30 integral scales but is only reached for  
400 larger rainfall rates with regard to the mean hydraulic conductivity.
- 401 4. The simple calculations of saturated area that might contribute to excess-infiltration  
402 generated runoff, based on hydraulic conductivity distributions at the land surface and  
403 rainfall rate, show poor agreement with the numerical simulations. Runoff  
404 parameterizations based upon these types of relationships would not be expected to  
405 produce accurate hydrographs.

406           While the inability of the simple relationships to predict saturated areas is discouraging,  
407 the ergodic behavior of the system for larger rainfall rates is not. This indicates that effective  
408 behavior might be reached at the hillslope scale. Analytic, stochastic approaches commonly  
409 applied to understand the role of subsurface heterogeneity on macrodispersion (e.g. Rubin and  
410 Dagan, 1992) might provide a template for understanding and upscaling Hortonian processes. In  
411 this manner, a new set of governing equations could be developed to represent small scale  
412 processes. Additionally, the changes in behavior shown in the presented numerical experiments  
413 should be used to guide field observations of hillslope runoff behavior. Coupling numerical  
414 experiments, theory and observations will yield a more complete understanding of the underlying  
415 processes.

416

#### 417 **Acknowledgements**

418 This work was performed partially under the auspices of the U.S. Department of Energy by  
419 Lawrence Livermore National Laboratory under contract W-7405-Eng-48.

420

#### 421 **References**

- 422 Ashby, S.F. and R.D. Falgout (1996). A parallel multigrid preconditioned conjugate gradient  
423 algorithm for groundwater flow simulations. *Nuclear Science and Engineering*, 124(1):145-59.
- 424 Binley, A., Elgy, J., Beven, K., (1989) A physically based model of heterogeneous hillslopes. 1.  
425 Runoff production. *Water Resources Research* 25 (6), 1219–1226.
- 426 Carle, S.F. and G.E. Fogg (1996) Transition probability-based indicator geostatistics,  
427 *Mathematical Geology*, 28(4): 453-476.
- 428 Carle, S.F. and G.E. Fogg (1997) Modeling Spatial Variability with One and Multidimensional  
429 Continuous-Lag Markov Chains, *Mathematical Geology*, 29(7): 891-918.

430 Dagan, G. (1989), *Flow and Transport in Porous Formations*, Springer-Verlag, New York.

431 Herbst, M., B. Diekkruger and J. Vanderborght (2006) Numerical experiments on the sensitivity  
432 of runoff generation to the spatial variation of soil hydraulic properties. *Journal of Hydrology*,  
433 326: 43-58.

434 Kollet S.J. and RM Maxwell (2006) Integrated surface-groundwater flow modeling: a free-  
435 surface overland flow boundary condition in a parallel groundwater flow model. *Advances in*  
436 *Water Resources*, 29(7): 945-958.

437 Liang, X., E.F. Wood, D.P. Lettenmaier (1996), Surface soil parameterization of the VIC-2L  
438 model: Evaluation and modification. *Global and Planetary Change*, 13: 195-206.

439 Lohmann, D., E. Raschke, B. Nijssen and D.P. Lettenmaier (1998), Regional scale hydrology: I.  
440 Formulation of the VIC-2L model coupled to a routing model. *Hydrologic Science Journal*,  
441 43:131-141.

442 Nahar, N., R.S. Govindaraju, C. Corradini and R. Morbidelli (2004) Role of runoff for describing  
443 field-scale infiltration and overland flow over spatially variable soils. *Journal of Hydrology*,  
444 286: 36-51.

445 Rubin, Y., and G. Dagan (1992) Conditional estimation of solute travel time in heterogeneous  
446 formations: Impact of transmissivity measurements, *Water Resources Research*, 28(4), 1033–  
447 1040.

448 Rubin, Y. (2003) *Applied Stochastic Hydrogeology* Oxford University Press.

449 Smith, L., and F. W. Schwartz, (1981) Mass transport, 2, A stochastic analysis of uncertainty in  
450 prediction, *Water Resources Research*, 17(2), 351–369.

451 Tompson, A. F. B., R. Ababou, and L. W. Gelhar (1989) Implementation of the three-  
452 dimensional turning bands random field generator, *Water Resources Research*, 25(10), 2227–  
453 2243.

454 Tompson, A. F. B., and L. W. Gelhar (1990) Numerical simulation of solute transport in three-  
455 dimensional randomly heterogeneous porous media, *Water Resources Research*, 26(10), 2541–  
456 2562.

457 Tompson, A. F. B., Falgout, R. D., Smith, S. G., Bosl, W. J., and Ashby, S. F. (1998), Analysis  
458 of subsurface contaminant migration and remediation using high performance computing:  
459 *Advances in Water Resources*, 22(3): 203-221

460 Wetzel, P.J., X. Liang, P. Irannejad, A. Boone, J. Noilhan, Y. Shao, C. Skelly, Y. Xue, Z-L Yang  
461 (1996), Modeling vadose zone liquid water fluxes: Infiltration, runoff, drainage, interflow.  
462 *Global and Planetary Change*, 13: 57-71.